Region stepwise reconstruction method based on two source–detector-separation groups for reconstructing background optical properties of two-layered slab sample

Ming Liu (刘 明)[1], Mengyu Jia (贾梦宇)[1], Huijuan Zhao (赵会娟)[1,2*], and Feng Gao (高 峰)[1,2]

[1]*College of Precision Instrument and Optoelectronics Engineering, Tianjin University, Tianjin 300072, China*
[2]*Tianjin Key Laboratory of Biomedical Detecting Techniques and Instruments, Tianjin 300072, China*
*Corresponding author: huijuanzhao@tju.edu.cn

The accuracy of the background optical properties has a considerable effect on the quality of reconstructed images in near-infrared functional brain imaging based on continuous wave diffuse optical tomography (CW-DOT). We propose a region stepwise reconstruction method in CW-DOT scheme for reconstructing the background absorption and reduced scattering coefficients of the two-layered slab sample with the known geometric information. According to the relation between the thickness of the top layer and source–detector separation, the conventional measurement data are divided into two groups and are employed to reconstruct the top and bottom background optical properties, respectively. The numerical simulation results demonstrate that the proposed method can reconstruct the background optical properties of two-layered slab sample effectively. The region-of-interest reconstruction results are better than those of the conventional simultaneous reconstruction method.

OCIS codes: 170.3880, 170.6960, 170.5280, 170.3660, 170.3010.
doi: 10.3788/COL201412.111702.

Near-infrared (NIR) functional brain imaging employing safe levels of optical radiation in the wavelength region of 650–900 nm primarily interrogates the changes in the absorption coefficient in the gray matter induced by brain activation and can potentially achieve spatial resolution of 10 mm in the adult human brain close to the skull[1]. In this field, diffuse optical tomography (DOT) substantially has greater spatial resolution and quantitativeness in comparison with optical topography. In the three schemes of DOT, the continuous wave (CW) method can provide fast data acquisition and great signal-to-noise level, and thus, it is widely used in near-infrared functional brain imaging.

Two-layered slab is still a reasonable simplified sample to the human brain in DOT, although more complex samples are proposed and occasionally applied to *in vivo* measurement data[2]. When the region of interest (ROI) induced by brain activation is reconstructed for the two-layered slab sample with DOT, it is generally assumed that: 1) the top layer represents the scalp and skull, while the bottom layer represents the gray matter; 2) the geometric information of the sample is known; 3) the background optical properties about the resting and the activation states are known and are identical. In the study on reconstructing ROI with the known background optical properties, some researchers demonstrated that CW-DOT scheme was able to reconstruct the absorption and reduced scattering coefficients simultaneously from the experimental and theoretical

point of view[3–6]. For the above-mentioned sample, the thickness of the scalp and skull can be obtained from the computerized tomography (CT) or magnetic resonance imaging (MRI) images of head. When an anatomical CT/MRI of the subject's head is not available, some researchers utilize the general template of top layer thickness to construct three-dimensional DOT images[7]. The background optical properties of the two-layered slab sample are derived from *in vitro* human brain tissues, which are different from those in living tissues[8]. It has been demonstrated that the quality of the reconstructed ROI images is affected by the uncertainty in the background optical properties and the restriction of the penetration depth of NIR light[9]. For this reason, some researchers attempt to reconstruct the background optical properties of two-layered slab; however, the reconstructed results are unsatisfactory[10]. Here the region stepwise reconstruction method (RSRM) is proposed for reconstructing the background optical properties of the two-layered slab sample with the known geometric information in CW-DOT scheme.

The basic principles of RSRM are as follows: owing to the limited depth resolution and the signal-to-noise ratio (SNR) of the source–detector separation (SDS), the SDSs range in the NIR functional brain imaging is approximately 10–50 mm and the depth of maximum brain sensitivity is approximately half the SDSs[11]. In the process of the reconstruction for the proposed method, we divide all the possible SDSs into two groups, that is, the short SDSs (S-SDS)

group and long SDSs (L-SDS) group, according to the relation between the thickness of top layer and the SDSs which has been investigated by Monte Carlo simulation[12]. The S-SDS is defined as the SDSs group that receives the measurement data of the photon density on the boundary (χ_{ds}) derived from the photons which almost pass only through the top layer (Region I); the L-SDS is defined as the SDSs group that receives the measurement data of the photon density on the boundary (χ_{dl}) derived from the photons which almost pass completely through the top layer and the bottom layer (Region II). Therefore, the process of reconstructing the top and bottom layer optical properties can utilize the information of χ_{ds} and χ_{dl}, respectively. We can select the appropriate S-SDS and L-SDS to receive χ_{ds} and χ_{dl}, on the condition that the thickness of the top layer has been known. According to the above analysis, RSRM is proposed to reconstruct the background optical properties of the top and bottom layers by using χ_{ds} and χ_{dl} respectively.

The CW diffusion equation (DE) is used to describe the propagation of photon in tissues based on highly scattering media and solved by the finite element method (FEM). DE is accordingly written as

$$\begin{cases} -(\nabla \cdot \kappa(r) + \mu_a(r))\Phi(r) = q(r), \\ \Phi(r) + 2\kappa(r)a\,e_n \cdot \nabla\Phi(r)\big|_{r \in \partial\Omega} = 0, \end{cases} \quad (1)$$

where $\mu_a(r)$ represents the absorption coefficient with r as the position vector; $\kappa(r) \approx 1/(3\mu_s'(r))$ represents the diffusion coefficient with $\mu_s'(r)$ as the reduced scattering coefficient; $\Phi(r)$ represents the photon density; $q(r)$ represents the photon density of the source; $\alpha = (1+R_f)/(1-R_f)$ with R_f as the internal reflection coefficient on the boundary; e_n is the outward unity vector normal to the tissue surface $\partial\Omega$. The photon density on the boundary is given by Fick's law with Robin boundary condition:

$$\Gamma(\xi_d, \zeta_s) = \frac{1}{2a}\Phi(\xi_d, \zeta_s), \quad (2)$$

where $\Gamma(\xi_d, \zeta_s)$ is the re-emitted density matrix on the multiple detectors at ξ_d ($d = 1, 2, ..., D$) when the tissue is stimulated by multiple sources at ζ_s ($s = 1, 2, ..., S$) on the boundary. In the inverse problem, the perturbation method can be employed to calculate the changes in optical properties:

$$\begin{bmatrix} J_a(\xi_d, \zeta_s) & J_s(\xi_d, \zeta_s) \end{bmatrix} \begin{bmatrix} \delta\mu_a \\ \delta\mu_s \end{bmatrix} = \delta\Gamma(\xi_d, \zeta_s)$$

$$= -\int_\Omega [\Gamma(\xi_d, r)\Phi(r, \zeta_s)\delta\mu_a(r) - \nabla\Gamma(\xi_d, r) \cdot \nabla\Phi(r, \zeta_s)3\kappa^2(r)\delta\mu_s'(r)]\mathrm{d}r, \quad (3)$$

where $J_a(\xi_d, \xi_s)$ and $J_s(\xi_d, \xi_s)$ are the Jacobian matrix of absorption and reduced scattering coefficients, respectively and $\delta\mu_a$, $\delta\mu_s$, and $\delta\Gamma(\xi_d, \zeta_s)$ are the perturbation of absorption coefficient, reduced scattering coefficient, and the re-emitted density.

During the reconstruction of the top layer background optical properties ($\mu_{a(I)}, \mu_{s(I)}$) with RSRM, we assume that the bottom background optical properties ($\mu_{a(II)}, \mu_{s(II)}'$)

are the same as those reconstructed in the top layer and the changes of the bottom background optical properties have no effect on χ_{ds}. On the condition that initial values are assigned to the top layer background optical properties, the above description can be written as the Newton–Raphson iteration form:

$$\begin{cases} \chi_{ds} - F(\mu_{a(I)}^i, \mu_{a(II)}^i, \mu_{s(I)}'^i, \mu_{s(II)}'^i) \\ = \left[\dfrac{1}{W_a}\sum_{e \in I} J_a^i(\xi_d, \zeta_s, e) \quad \dfrac{1}{W_s}\sum_{e \in I} J_s^i(\xi_d, \zeta_s, e)\right] \begin{bmatrix} W_a\delta\mu_a^i \\ W_s\delta\mu_s'^i \end{bmatrix}, \\ W_a = \max_{e \in I}\left|J_a^i(\xi_d, \zeta_s, e)\right|, \quad W_s = \max_{e \in I}\left|J_s^i(\xi_d, \zeta_s, e)\right|, \\ \mu_{a(I)}^{i+1} = \mu_{a(II)}^{i+1} = \mu_{a(I)}^i + \delta\mu_a^i, \; \mu_{s(I)}'^{i+1} = \mu_{s(II)}'^{i+1} = \mu_{s(I)}'^i + \delta\mu_s'^i, \quad (4) \end{cases}$$

where $F(\bullet)$ represents the re-emitted density on the boundary calculated by the forward problem; i is the number of iterations; $J_s(\xi_d, \xi_s, e)$ and $J_a(\xi_d, \xi_s, e)$ are the Jacobian matrix elements of the small voxel e in FEM; W_a and W_s are scale normalization factors to balance the Jacobian matrix elements, which are equal to the absolute maximums of $J_s(\xi_d, \xi_s, e)$ and $J_a(\xi_d, \xi_s, e)$ in an iterative computation.

After the determination of $\mu_{a(I)}$ and $\mu_{s(I)}'$ from Eq. (4), we utilize χ_{dl} obtained from L-SDS to reconstruct the bottom optical properties. Now $\mu_{a(I)}$ and $\mu_{s(I)}'$ are regarded as the true values of the top layer and do not update by the forward problem. The inverse calculation of $\mu_{a(II)}$ and $\mu_{s(II)}'$ is described as

$$\begin{cases} \chi_{dl} - F(\mu_{a(I)}, \mu_{a(II)}^i, \mu_{s(I)}', \mu_{s(II)}'^i) \\ = \left[\dfrac{1}{W_a}\sum_{e \in II} J_a^i(\xi_d, \zeta_s, e) \quad \dfrac{1}{W_s}\sum_{e \in II} J_s^i(\xi_d, \zeta_s, e)\right] \begin{bmatrix} W_a\delta\mu_a^i \\ W_s\delta\mu_s^i \end{bmatrix}, \\ W_a = \max_{e \in II}\left|J_a^i(\xi_d, \zeta_s, e)\right|, \quad W_s = \max_{e \in II}\left|J_s^i(\xi_d, \zeta_s, e)\right|, \\ \mu_{a(II)}^{i+1} = \mu_{a(II)}^i + \delta\mu_a^i, \quad \mu_{s(II)}'^{i+1} = \mu_{s(II)}'^i + \delta\mu_s'^i. \quad (5) \end{cases}$$

With the above procedures, the background optical properties of two-layered slab sample are calculated by RSRM.

In the following, we demonstrate the existence and investigate the range of the SDSs group by the numerical simulations. A slab is adopted with the dimensions of $W = 60$, $L = 60$, $H = 30$ mm, and the top layer has the thickness $h = 10$ mm as shown in
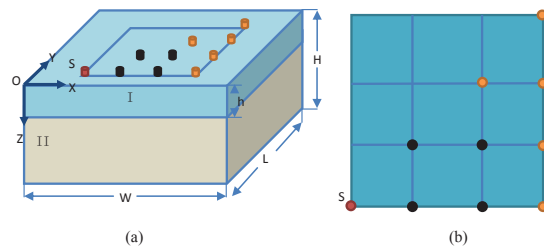

(a)   (b)

Fig. 1(a) Two-layered slab sample. (b) Source–detector distribution to reconstruct the background optical properties by RSRM with the source locating at the point of S. ● represents the location of S-SDS and ● represents the detector location of L-SDS.

Table 1. Reconstructed Results of Top Layer Background Optical Properties Using Three SDSs Group for $h = 10$ mm

	$\mu_{a(I)}(\mathrm{mm}^{-1})$	$\mu'_{s(I)}(\mathrm{mm}^{-1})$
Group 1	0.0158	1.92
Group 2	0.0158	1.91
Group 3	0.0157	1.91

Fig. 1(a). The true values of the background optical properties are set at $\mu_{a(I)} = 0.015$ mm^{-1}, $\mu'_{s(I)} = 2.0$ mm^{-1}, $\mu_{a(II)} = 0.02$ mm^{-1}, and $\mu'_{s(II)} = 1.2$ mm^{-1}, by referring the values in Ref. [13]. The source and detectors are arranged at a square area of 30×30 (mm) at the center of the top surface as shown in Fig. 1(b), and the shortest distance between two points is set at 10 mm according to the thickness of the top layer. The iterative initial values would affect the calculating speed and the convergence of the solution on the numerical calculation of the Newton–Raphson iteration. For simplicity, we set the initial values at the possible minimum values $\mu'_{a(I)}=0.005\,\mathrm{mm}^{-1}$, $\mu'_{a(II)}=0.01\,\mathrm{mm}^{-1}$, and $\mu'_{s(I)}=\mu'_{s(II)}=0.6\,\mathrm{mm}^{-1}$ by referring the values in Refs. [2, 14]. The measurement on the boundary is generated using the true values from the forward problem. The iterative error is defined as $\varepsilon = \sum\limits_{s=1}^{S}\sum\limits_{d=1}^{D}\left[\dfrac{\chi_{s,d} - F_{s,d}}{\chi_{s,d}}\right]^2$ which evaluates the closeness between the reconstructed results $F_{s,d}$ and the measurement data $\chi_{s,d}$ at the detectors, and the terminated condition is set at $\left|\dfrac{\varepsilon_i - \varepsilon_{i+1}}{\varepsilon_{i+1}}\right| < 0.01$.

The regularization method adopts ART algorithm[15,16], and the programming environment utilizes COMSOL 4.3 with MATLAB 2012a.

Firstly, we determine the range of the S-SDS. To the sample with the top layer thickness $h = 10$ mm as shown in Fig. 1(a), S-SDS can adopt three SDSs groups representing as Group 1 (10, 14.1 mm), Group 2 (10, 14.1, 20 mm), and Group 3 (10, 14.1, 20, 22.4 mm) as shown in Fig. 1(b). In order to determine the reasonable S-SDS, the top layer background optical properties are reconstructed with RSRM. The results are shown in Table 1.

According to our purpose, the maximum depth range explored by detectors of S-SDS should not reach the bottom layer tissue but cover the top layer tissue as far as possible. It can be seen from Table 1 that the difference in the reconstructed results is relatively small. For the purpose of application, the S-SDS with the larger detection range should be selected due to the inhomogeneity of human tissue. Thus, we select (10, 14.1, 20, 22.4 mm) as S-SDS.

Secondly, we investigate the influence of the top layer thickness variation on the reconstructed results with the above S-SDS, since a helmet with the fixed SDS is usually adopted for different subjects. Considering the SNR of the DOT system, the maximum SDS is generally less than 50 mm, thus L-SDS is set at (28.3, 30, 31.6, 36.1, 42.4 mm). Considering the spatial resolution of NIR functional brain DOT in millimeters and the general top layer thickness of an adult head, the top layer thickness h is changed from 5 to 14 mm in a step of 1 mm. The reconstructed results are shown in Table 2.

Table 2. Reconstructed Results of Background Optical Properties and Related Errors Using RSRM with Different Top Layer Thicknesses

	$\mu_{a(I)}(\mathrm{mm}^{-1})$ /(rel. err.)	$\mu'_{s(I)}(\mathrm{mm}^{-1})$ /(rel. err.)	$\mu_{a(II)}(\mathrm{mm}^{-1})$ /(rel. err.)	$\mu'_{s(II)}(\mathrm{mm}^{-1})$ /(rel. err.)
5 mm	0.0155/(3.3%)	1.87/(6.5%)	0.0201/(0.5%)	1.25/(4.2%)
6 mm	0.0158/(5.3%)	1.92/(4.0%)	0.0198/(1.0%)	1.24/(3.3%)
7 mm	0.0157/(4.7%)	1.91/(4.5%)	0.0196/(2.0%)	1.23 /(2.5%)
8 mm	0.0157/(4.7%)	1.93/(3.5%)	0.0191/(4.5%)	1.21/(1.0%)
9 mm	0.0157/(4.7%)	1.91/(4.5%)	0.0193/(3.5%)	1.22/(1.7%)
10 mm	0.0158/(5.3%)	1.91/(4.5%)	0.0192/(4.0%)	1.19/(1.0%)
11 mm	0.0160/(5.3%)	1.92/(4.0%)	0.0183/(8.5%)	1.18/(1.7%)
12 mm	0.0160/(6.7%)	1.92/(4.0%)	0.0179/(10.5%)	1.17/(2.5%)
13 mm	0.0160/(6.7%)	1.92/(4.0%)	0.0172/(14.0%)	1.14/(5.0%)
14 mm	0.0160/(6.7%)	1.91/(4.5%)	0.0140/(30%)	1.68/(40%)

Table 3. Reconstructed Results of Background Optical Properties and Related Errors with Thickness Deviation of the Top Layer

	$\mu_{a(I)}(mm^{-1})$ /(rel. err.)	$\mu'_{s(I)}(mm^{-1})$ /(rel. err.)	$\mu_{a(II)}(mm^{-1})$ /(rel. err.)	$\mu'_{s(II)}(mm^{-1})$ /(rel. err.)
−20%	0.01608/(7.2%)	1.931/(3.5%)	0.01686/(15.7%)	1.112/(7.3%)
−10%	0.01606/(7.1%)	1.927/(3.7%)	0.01785/(10.8%)	1.159/(3.4%)
10%	0.01599/(6.6%)	1.919/(4.1%)	0.01897/(5.2%)	1.243/(3.6%)
20%	0.01597/(6.5%)	1.917/(4.2%)	0.01778/(11.1%)	1.138/(5.2%)

It can be seen from Table 2 that RSRM can reconstruct the background optical properties effectively with the above S-SDS and L-SDS. For reconstruction of $\mu_{a(I)}$ and $\mu'_{s(I)}$, it is suggested that if h increases, the reconstruction ability with S-SDS slightly abates. When h is more than 11 mm, the reconstructed results of the top layer hardly change with the variation of h, which may suggests that the maximum depth range of S-SDS is between 10 and 11 mm. For the reconstruction of $\mu_{a(II)}$ and $\mu'_{s(II)}$, as shown in the third and fourth columns of Table 2, increase in the top layer thickness is the main factor affecting the accuracy of the bottom layer result. The improvement of bottom layer reconstruction for small SDSs is ascribed to the accurate optical property reconstruction of the top layer with RSRM. When h is equal to 14 mm, the reconstruction error is more than 30%.

Thirdly, we investigate the influence of the errors in the thickness of top layer, which comes from the irregular geometric shapes of the brain. Assuming that the thickness deviations are ±10% and ±20% of $h = 10$ mm, the background optical properties are reconstructed by RSRM as shown in Table 3.

It can be seen from Table 3 that the related errors of the top layer are relatively stable between 4.0% and 8.0%. The bottom layer related errors are significantly greater than those of the top layer and increase with the increase in the thickness deviation of the top layer. As shown in Tables 2 and 3, the reconstruction ability of the bottom background abates with the increase in the top layer thickness to some degree. In future studies, enhancing the ability of RSRM in the depth reconstruction is the key point. Furthermore, we reconstruct the samples with some other true values of the background optical properties and initial

iteration values with RSRM, which also come to similar conclusions.

To further validate the effectiveness of RSRM, we compare RSRM with the simultaneous reconstruction (SR) which adopts the measurement data from all the possible source–detector pairs and reconstructs the optical properties of the two layers simultaneously. Considering the system noise with the instrument, the SNR of the DOT system is generally greater than 40 dB. The noise with SNR of 40 dB is added to the measurement data written as: $\Gamma = \overline{\Gamma}(1 + 10^{\frac{-SNR}{20}} G_{noise})$, where $\overline{\Gamma}$ represents original data without noise and G_{noise} is the Gaussian white noise.

As can be seen in Table 4, the reconstruction results using RSRM are much better than those obtained from SR. Since the resolution of CW-DOT degrades rapidly with increasing depth in the sample, the top and bottom layer reconstructed information is reciprocally affected with SR. The bottom optical properties are more difficult to be accurately reconstructed by SR due to the difference in the reconstruction capacity
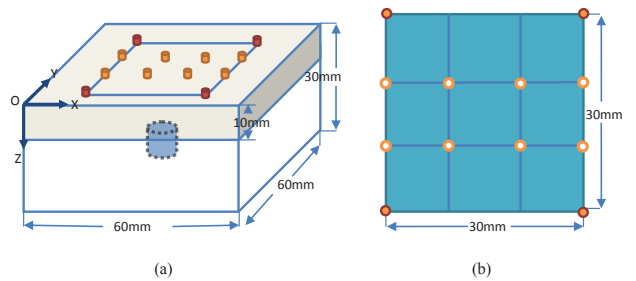

Fig. 2(a) Sample with the target of ROI. (b) Source–detector distribution used to reconstruct ROI. The sources locate at points of ● and the detectors locate at points of ○ and ●.

Table 4. Reconstruction Results of Two-layered Slab Sample Comparing RSRM with SR

	$\mu_{a(I)}(mm^{-1})$/(err.)	$\mu'_{s(I)}(mm^{-1})$/(err.)	$\mu_{a(II)}(mm^{-1})$/(err.)	$\mu'_{s(II)}(mm^{-1})$/(err.)
SR	0.0170/(13.3%)	1.85/(7.5%)	0.0146/(27.0%)	1.60/(33.3%)
RSRM	0.0160/(6.7%)	1.92/(4.0%)	0.0186/(7.0%)	1.22/(1.7%)

(a)

(b)
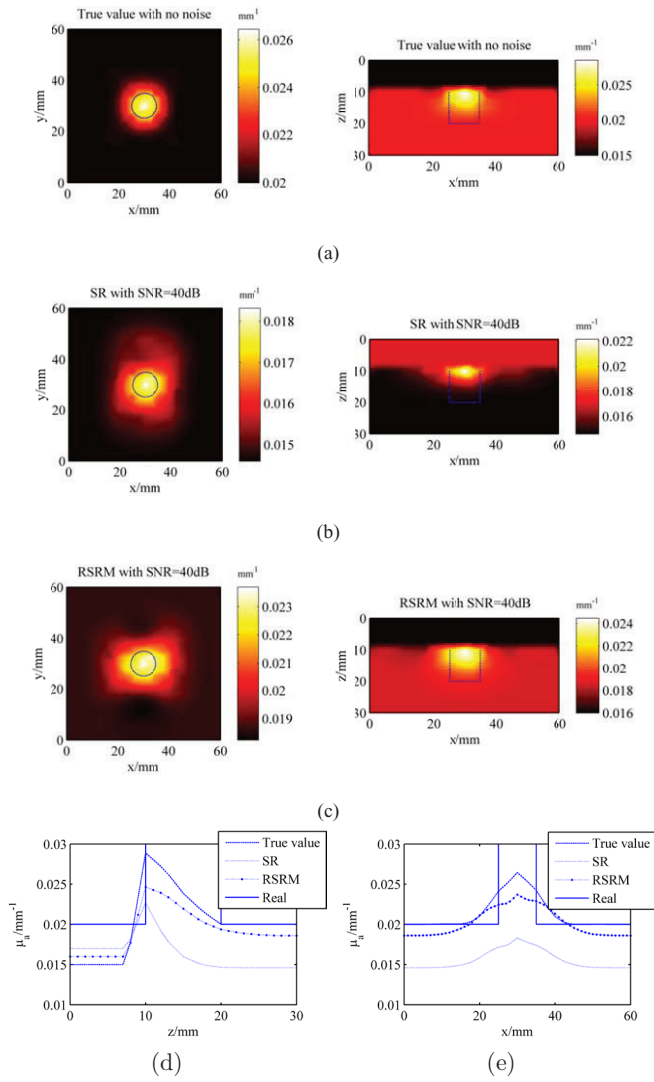
(c)

(d)   (e)

Fig. 3(a) Reconstructed ROI images with the true background optical properties. ROI reconstruction images with the background optical properties reconstructed by (b) SR and (c) RSRM, respectively. The dashed line denotes the true location and size of ROI. Y and X profile of (d) X, Y sectional images at $y = 30$ and (e) X, Z sectional images at $x = 30$ mm.

of the SDSs groups. But RSRM divided the original reconstruction into two processes and achieved stepwise to reduce the influence of each layer, which improves the quality of the reconstruction results.

Based on the above observation, the improvement of the RSRM on the reconstruction of target caused by

brain activation is investigated. Only the changes in absorption coefficient of ROI are reconstructed, since the changes in reduced scattering coefficient are generally negligible during brain activation. We assume that the ROI is cylindrical in shape with 5 mm radius and 10 mm height. The cylinder is assumed just below the top layer and located in the center of the X–Y plane as shown in Fig. 2(a), $\Delta\mu_a$ is set at 0.02 mm^{-1}[2]. Source–detector distribution uses four L-SDSs as shown in Fig. 2(b). Three groups of ROI reconstruction images are displayed with different background optical properties, which are the true background optical properties with no noise of the measurement data under ideal conditions as shown in Fig. 3(a) and the background optical properties reconstructed by SR and RSRM with SNR = 40 dB as shown in Figs. 3(b) and (c), respectively. Matlab interpolation function is adopted in figures plotted owing to the discrete node points calculated by FEM. In Fig. 3 X, Y sectional images are at $z = 12.5$ mm, X, Z sectional images are at $y = 30$ mm; Y profile is along $y = 30$ mm of X, Y sectional images and X profile is along $x = 30$ mm of X, Z sectional images as shown in Figs. 3(d) and (e).

On the condition that the background optical properties cannot be known accurately, the location and size of ROI reconstructed can be exactly identified from SR and the RSRM. But the area of ROI is obvious smaller in X, Z sectional images from SR than that from RSRM. Furthermore, we evaluate the reconstructions in terms of the quantitativeness ratio (QR), full-width at half-maximum (FWHM), and effective reconstruction depth (ERD) as shown in Table 5. QR is defined as the ratio of the difference between the maximum of the reconstructed μ_a and background μ_a to the difference between the original μ_a of ROI and background μ_a in X, Y sectional images. ERD is defined as the maximal depth as the reconstructed results are equal to half of the maximum reconstructed value of ROI of X, Z sectional images. Comparing ROI reconstruction results from the RSRM with those under the ideal condition, it is found that the percentage of QR is 45%, FWHM is 16, and ERD is the same. Comparing the results from the RSRM with those from the SR, it is found that QR is 24%, FWHM is the same, and ERD is 13. It indicates that the ROI reconstruction quality from the RSRM is higher than that from the SR as the background optical properties cannot be known accurately.

Table 5. Comparison of the Reconstruction Quality with Background Optical Properties Between SR and RSRM

	QR	FWHM (mm)	ERD (mm)
True Value with No Noise	64%	12	15
SR with SNR = 40 dB	24%	16	13
RSRM with SNR = 40 dB	45%	16	15

In conclusion, knowledge of background optical properties is essential for the accurate reconstruction of target in the NIR functional brain imaging using CW-DOT scheme. We propose RSRM to reconstruct the background optical properties of top and bottom layers of a two-layered sample with S-SDS and L-SDS, respectively. We also test the effectiveness of the method with numerical simulations and find that it can reconstruct the background optical properties' relative error less than 7.0% with SNR = 40 dB. We reconstruct the change in absorption coefficient of ROI with different background optical properties and find that the ROI reconstruction quality is better in reconstructing ROI with the background optical properties calculated by this method than that from SR in terms of QR and ERD. For determination of S-SDS, it is suggested that it can be selected from h to $2h$ for the normal SDSs of 10–50 mm. For the SDS larger than but approximately equal to 2h, they can be ranged into S-SDS or not due to the fact that the choice has less influence on the reconstruction accuracy of the top layer optical properties. As the proposed RSRM has no limit to the forward model, RSRM is also applicable to frequency domain DOT and time domain DOT system.

References

1. D. A. Boas, A. M. Dale, and M. A. Franceschini, NeuroImage **23,** S275 (2004).
2. J. Selb, T. M. Ogden, J. Dubb, Q. Fang, and D. A. Boas, J. Biomed. Opt. **19,** 016010 (2014).
3. Y. Xu, X. Gu, T. Khan, and H. Jiang, Appl. Opt. **41,** 25 (2002).
4. S. Srinivasan, B. W. Pogue, S. Jiang, H. Dehghani, and K. D. Paulsen, Appl. Opt. **44,** 10 (2005).
5. A. Corlu, R. Choe, T. Durduran, K. Lee, M. Schweiger, S. R. Arridge, E. M. C. Hillman, and A. G. Yodh, Appl. Opt. **44,** 11 (2005).
6. B. Harrach, Inverse Probl. **25,** 055010 (2009).
7. A. Custo, D. A. Boas, D. Tsuzuki, I. Dan, R. Mesquita, B. Fischl, W. E. L. Grimson, and W. Wells, NeuroImage **49,** 561 (2010).
8. M. Dehaes, P. E. Grant, D. D. Sliva, N. R. Labarbe, R. Pienaar, D. A. Boas, M. A. Franceschini, and J. Selb, Biomed. Opt. Express **552,** 3 (2011).
9. X. Cheng and D. A. Boas, Opt. Express **299,** 8 (1999).
10. M. Shimada, C. Sato, Y. Hoshi, and Y. Yamada, Phys. Med. Biol. **54,** 5057 (2009).
11. G. Strangman, D. A. Boas, and J. P. Sutton, Biol. Psychiatry **52,** 679 (2002).
12. C. Lee, C. Sun, P. Lee, H. Lee, C. C. Yang, C. Jiang, Y. Tong, T. Yeh, and J. Hsieh, Opt. Express **8339,** 21 (2005).
13. F. Gao, H. Zhao, Y. Tanikawa, and Y. Yamada, Phys. Med. Biol. **49,** 1055 (2004).
14. A. N. Yaroslavsky, P. C. Schulze, I. V. Yaroslavsky, R. Schober, F. Ulrich, and H. J. Schwarzmaier, Phys. Med. Biol. **47,** 2059 (2002).
15. Y. Ma, F. Gao, P. Ruan, F. Yang, and H. Zhao, Chin. Opt. Lett. **8,** 787 (2010).
16. M. Jia, S. Cui, X. Chen, M. Liu, X. Zhou, H. Zhao, and F. Gao, Chin. Opt. Lett. **12,** 031702 (2014).